

Electrokinetic Propulsion for Electronically Integrated Microscopic Robots

Lucas C. Hanson^{1†}, William H. Reinhardt^{2†}, Scott Shrager¹, Tarunyaa Sivakumar² and Marc Z. Miskin^{2*}

¹Department of Physics and Astronomy, University of Pennsylvania, Philadelphia, 19104, PA, USA.

²Department of Electrical and Systems Engineering, University of Pennsylvania, Philadelphia, 19104, PA, USA.

*Corresponding author(s). E-mail(s): mmiskin@seas.upenn.edu;

Contributing authors: lhanson@sas.upenn.edu;
whr@seas.upenn.edu; sshrager@wharton.upenn.edu;
tarunyaa@seas.upenn.edu;

†These authors contributed equally to this work (listed alphabetically).

Abstract

Robots too small to see by eye have rapidly evolved in recent years thanks to the incorporation of on-board microelectronics. Semiconductor circuits have been used in microrobots capable of executing controlled wireless steering [1, 2], prescribed legged gait patterns [1, 2], and user-triggered transitions between digital states [2]. Yet these promising new capabilities have come at the steep price of complicated fabrication. Even though circuit components can be reliably built by semiconductor foundries, currently available actuators for electronically integrated microrobots are built with intricate multi-step cleanroom protocols and use mechanisms like articulated legs [1, 2] or bubble generators [3–5] that are hard to design and control. Here, we present a propulsion system for electronically integrated microrobots that can be built with a single step of lithographic processing, readily integrates with microelectronics thanks to low current/low voltage operation (1V, 10nA), and yields robots that swim at speeds over one body length per second. Inspired by work on micromotors, these robots generate electric fields in a surrounding fluid, and by extension propulsive electrokinetic flows [6–11]. The underlying physics is captured by a model in

which robot speed is proportional to applied current, making design and control straightforward. As proof, we build basic robots that use on-board circuits and a closed-loop optical control scheme to navigate waypoints and move in coordinated swarms. Broadly, solid-state propulsion clears the way for robust, easy to manufacture, electronically controlled microrobots that operate reliably over months to years.

The basic mechanisms behind electrokinetic propulsion [12, 13] are depicted in Figure 1a. The motor generates an electric field by feeding current into solution. This field pushes on mobile charges nearby the robot (e.g., in the electrical double layer surrounding the motor and/or nearby surfaces or the diffusion layer). Movement of the charges is resisted by drag from the surrounding fluid, establishing a flow that moves the motor.

In general, electrokinetic propulsion has several attractive features for electronically integrated microrobots. Prior work on electrokinetic micromotors has shown high speed propulsion (> 1 body length per second) while consuming low power ($\sim 10^{-15}$ W) [14–16]. Further, many of the materials used in micromotors, like refractory metals and metal-oxides, are compatible with clean room processing [6, 17], enabling straightforward integration. Finally, the voltages and currents are limited by electrochemistry in the surrounding solution to approximately 0.1-1 V and 10 pA/ μm^2 , respectively, making them compatible with semiconductor circuits [18–24].

To realise these potential gains, we built a prototype robot that generates its propulsive electric field using on-board electronics (Fig. 1b). Photovoltaic (PV) cells, wired in series, feed current into the solution through 70 x 70 μm titanium-platinum electrodes at either end of the robot. For insulation, the PVs and associated wiring are covered in a layer of photoresist. All of these parts are fabricated massively in parallel with a previously developed, fully lithographic protocol [1, 2], enabling several hundred devices per 1 cm chip as seen in Figure 1b.

Once released into solution and illuminated, the robot moves at a steady speed, oriented with the positive electrode in the front (Fig. 1c and Supplementary Video 1). Note, the robot moves along the bottom surface of the container it is in, as it is negatively buoyant. We independently measure the current produced by the PVs under various illumination conditions (see Methods) and find the robot’s speed is proportional to current density and inversely proportional to solution conductivity, σ (Extended Data Fig. E1). Indeed when speed is plotted against the electric field (i.e. the ratio of current density to conductivity), the data collapse to a single line, as shown in the upper inset of Figure 2a.

Aside from conductivity, we find propulsion speed is largely independent of the surrounding chemical environment. Figure 2a shows robots can move in a variety of solutions, including two decades of different hydrogen peroxide concentrations, deionized water ($\sigma = 250$ nS/cm), salt solutions ($\sigma = 10$

$\mu\text{S}/\text{cm}$), pH buffers (5.5 to 8), and formaldehyde. We also find robots move on a variety of substrates, including polystyrene, oxygen plasma cleaned glass, positive charge functionalized glass, SU-8 photoresist films, platinum, and through microfluidic channels (see Supplementary Video 2). In every case, the relationship between speed and electric field is linear, with the slope alone coupled to the chemical environment (Fig. 2a). This effect is also small: the highest effective mobility (10 mM hydrogen peroxide) and the lowest (deionized water) only differ by a factor of 3. By contrast, the speed of the robots can be changed by more than two orders of magnitude through electronic control of the current.

To better analyze the underlying fluid dynamics, we image propulsion from the side, directly measuring the robot’s three degrees of freedom: speed, angle of attack, and gap height above the substrate (see Supplementary Video 3). As shown in Figure 2, each parameter increases as the field gets larger. Given the three kinematic constraints from force and torque equilibrium, a model can be constrained to predict a unique solution for the robot’s configuration.

We find three physical ingredients are sufficient to predict the trends in Figure 2. First, we make a lubrication approximation, assuming fluid forces are largest in the small gap between the robot and substrate. All other forces from the fluid are lumped into a small phenomenological forcing term derived by symmetry considerations. Second, we assume the electric field dominantly points along the axis running from the positive to negative electrode. Third, we use the “standard model” of electrokinetics [12, 13], which couples the fluid to the electric field by imposing a boundary slip condition $\Delta U = \beta \vec{E}$, where β is the slip coefficient for that surface. We numerically solve the governing fluid and electrical field equations in the gap under the robot (see Methods) and impose force and torque balance to identify equilibrium angle and gap height at a given electric field strength.

Fitting the model produces the black traces in Figure 2b and Figure 2c, which agree with the data. Further, the fit parameters are consistent with the underlying physics. For instance, the difference in mobility between the robot’s body and the substrate is a free parameter in the model and the best fit result is within the range of literature values for the mobility of silicon dioxide and polystyrene in aqueous solutions at similar pH values [25, 26]. We note this model is distinct from those used to describe micromotors because we are operating at a much larger length scale: whereas micromotors can have features on the order of the Debye length (here $\sim 10 - 100$ nm), our robots are over three orders of magnitude larger in size and thus in the “thin Debye layer” limit. Further discussion is included in the Methods section.

Compared to existing micromotors, the devices shown here offer several improvements. Many motors such as bimetallic nanorods or Janus particles, while elegant in their simplicity, operate at small sizes, low energy scales [14, 27, 28], and are strongly tied to environmental chemistry for propulsion. By contrast, electronic control of the current flowing through solution lifts these constraints, enabling operation in a range of environments and at larger sizes and energy scales. For example, the robots presented here operate at fields

nearly two orders of magnitude larger than chemically driven motors [28]. By extension, the robot retains the ability to propel at roughly one body length per second, despite the fact that it is more than one hundred fold larger in size.

While the single motor robot depicted in Figure 1c swims straight, the linear relationship between speed and current provides a direct route to controlled steering: attach two motors together and independently vary the current supplied to each [29]. To do this, we use a spatial light modulator (SLM) in the closed-loop control scheme shown in Figure 3a. This setup generates optical patterns of high and low intensity light in the microscope field of view to power individual motors (see Methods). A computer detects the robot positions and generates new optical patterns based on the image data and user prescribed control laws. This process runs autonomously, tracking robots and shooting light at them as they move.

By studying the robot’s behavior under different proportions of optical power, we find that when two engines are joined together, the motion is governed by differential drive kinematics. Specifically, in a differential drive system the left and right side of a robot move at different velocities (V_L and V_R , respectively), resulting in a forward velocity equal to their average and a rate of turning, or curvature, proportional to their normalized difference $\eta = (V_L - V_R)/(V_L + V_R)$ (Fig. 3b) [30]. Because the speed of a motor is proportional to the optical power incident upon it (Extended Data Fig. E2), we can compare the predictions for differential drive kinematics to the measured data, as shown in Figure 3c. Accounting for partial illumination between motors due to imperfect focusing of the light pattern (see Methods), we find agreement between the predicted kinematics and experimental data without fit parameters.

Differential drive systems can be directly controlled by a variety of well understood laws, allowing us to reliably position robots in space and time. To demonstrate, we implement two control laws (see Methods) to direct our robots through a series of waypoints [31, 32]. Both controllers proportionally adjust engine power using the angle between the robot’s heading and a vector that points from the robot’s center of mass to the target position, denoted by θ in Figure 3. One controller adjusts both motors simultaneously while the other only adjusts the power on the motor further from alignment. Both controllers readily guide robots through prescribed patterns. Figure 3d shows the dual-motor controller directing a robot to a target location (Supplementary Video 4) while Figure 3e (Supplementary Video 5) shows the single motor controller driving a robot around a “Figure 8” pattern.

Beyond single robots, optical control can be used to simultaneously pilot multiple devices. In Figure 4a and Figure 4b, we generate a list of waypoints and assign each one to the nearest robot. The robots simultaneously travel to their unique waypoints, rearranging the overall system to form user defined shapes, here lines and triangles (Supplementary Videos 6-7). Furthermore, each robot can be given its own list of waypoints in order to have multiple robots perform separate tasks. We demonstrate this in Figure 4c and Supplementary

Video 8 by having three robots swim in unison on different paths. Last, as seen in Figure 4d, waypoints can be dynamic, evolving with the swarm: here, we create a chain of robots following a leader by assigning each robot to follow a neighboring device in the chain (Supplementary Video 9). These results show double the number of microrobots under simultaneous, independent control than has been previously demonstrated in the literature [33–38]. However, we estimate that this approach can be scaled up to control an order of magnitude more robots, due to the ability to pattern light up to the resolution limit of the SLM (see Methods) [39].

Compared to other electronically integrated microrobots, the devices shown here are primitive. They carry only the bare minimum circuitry necessary to move, have no sensing capability, carry no internal computation, and cannot communicate. Yet they are vastly easier to build and more robust than alternative approaches to actuation, requiring only a single step of lithographic patterning for the entire propulsion system. The actuator itself is a chemically stable, but more or less arbitrary metal electrode, requiring few material considerations, no atomically thin material layers, and no 3D self-folding construction [2, 40, 41].

The simplicity of this approach confers broad robustness. We find devices can last for upwards of a year in solution, can be transferred with macroscopic pipettes upwards of one hundred times, and can be dried and re-immersed without loss of function. This stability marks a major improvement over other robots we have built using electrochemical actuators [1, 2] or bubble generators, which are far easier to damage, and typically last for a few weeks at most.

Improvements in stability, fabrication and control are crucial in moving microrobots towards real-world applications. Electrokinetic propulsion delivers these advantages, but without sacrificing the capacity to readily integrate electronics. Further integration with sophisticated circuits could help realize a best-of-both worlds scenario, in which the high speeds and robust performance inherent to micromotors could be mixed with the powerful sensing and computational capabilities of integrated electronics. For instance, propulsive current could be regulated by on-board silicon systems for sensing, control, or computation instead of the optical system used here. Indeed, the control laws that govern differential drive require only a handful of components to implement and the power and voltage requirements are within the ranges of previously demonstrated computing systems for micro-robotics [42]. These results point to a promising, near term future, in which microrobots use solid-state propulsion to carry out long-term, complex tasks with full autonomy.

References

- [1] Marc Z. Miskin, Alejandro J. Cortese, Kyle Dorsey, Edward P. Esposito, Michael F. Reynolds, Qingkun Liu, Michael Cao, David A. Muller, Paul L. McEuen, and Itai Cohen. Electronically integrated, mass-manufactured, microscopic robots. *Nature*, 584(7822):557–561, August 2020. Number:

7822 Publisher: Nature Publishing Group.

- [2] Michael F. Reynolds, Alejandro J. Cortese, Qingkun Liu, Zhangqi Zheng, Wei Wang, Samantha L. Norris, Sunwoo Lee, Marc Z. Miskin, Alyosha C. Molnar, Itai Cohen, and Paul L. McEuen. Microscopic robots with onboard digital control. *Science Robotics*, 7(70):eabq2296, September 2022. Publisher: American Association for the Advancement of Science.
- [3] Alexander A. Solovev, Yongfeng Mei, Esteban Bermúdez Ureña, Gaoshan Huang, and Oliver G. Schmidt. Catalytic Microtubular Jet Engines Self-Propelled by Accumulated Gas Bubbles. *Small*, 5(14):1688–1692, 2009. eprint: <https://onlinelibrary.wiley.com/doi/pdf/10.1002/smll.200900021>.
- [4] Vladimir M. Fomin, Markus Hippler, Veronika Magdanz, Lluís Soler, Samuel Sanchez, and Oliver G. Schmidt. Propulsion Mechanism of Catalytic Microjet Engines. *IEEE Transactions on Robotics*, 30(1):40–48, February 2014. Conference Name: IEEE Transactions on Robotics.
- [5] Qingjia Chi, Zhen Wang, Feifei Tian, Ji’an You, and Shuang Xu. A Review of Fast Bubble-Driven Micromotors Powered by Biocompatible Fuel: Low-Concentration Fuel, Bioactive Fluid and Enzyme. *Micromachines*, 9(10):537, October 2018.
- [6] Jie Zhang, Bartosz A. Grzybowski, and Steve Granick. Janus Particle Synthesis, Assembly, and Application. *Langmuir*, 33(28):6964–6977, July 2017. Publisher: American Chemical Society.
- [7] Andrew I. Campbell, Stephen J. Ebbens, Pierre Illien, and Ramin Golestanian. Experimental observation of flow fields around active Janus spheres. *Nature Communications*, 10(1):3952, September 2019. Number: 1 Publisher: Nature Publishing Group.
- [8] Michael Kuron, Patrick Kreissl, and Christian Holm. Toward Understanding of Self-Electrophoretic Propulsion under Realistic Conditions: From Bulk Reactions to Confinement Effects. *Accounts of Chemical Research*, 51(12):2998–3005, December 2018. Publisher: American Chemical Society.
- [9] Jeffrey L. Moran and Jonathan D. Posner. Phoretic Self-Propulsion. *Annual Review of Fluid Mechanics*, 49(1):511–540, January 2017.
- [10] Allan M. Brooks, Mykola Tasinkevych, Syeda Sabrina, Darrell Velezol, Ayusman Sen, and Kyle J. M. Bishop. Shape-directed rotation of homogeneous micromotors via catalytic self-electrophoresis. *Nature Communications*, 10(1):495, January 2019. Publisher: Nature Publishing Group.

- [11] Wei Wang, Wentao Duan, Ayusman Sen, and Thomas E. Mallouk. Catalytically powered dynamic assembly of rod-shaped nanomotors and passive tracer particles. *Proceedings of the National Academy of Sciences*, 110(44):17744–17749, October 2013.
- [12] J. Lyklema. *Fundamentals of interface and colloid science*. Academic Press, San Diego, 2000.
- [13] Robert J. Hunter. *Foundations of colloid science*. Oxford University Press, Oxford ; New York, 2nd ed edition, 2001.
- [14] Wei Wang, Tso-Yi Chiang, Darrell Velegol, and Thomas E. Mallouk. Understanding the Efficiency of Autonomous Nano- and Microscale Motors. *Journal of the American Chemical Society*, 135(28):10557–10565, July 2013. Publisher: American Chemical Society.
- [15] Walter F. Paxton, Paul T. Baker, Timothy R. Kline, Yang Wang, Thomas E. Mallouk, and Ayusman Sen. Catalytically Induced Electrokinetics for Motors and Micropumps. *Journal of the American Chemical Society*, 128(46):14881–14888, November 2006. Publisher: American Chemical Society.
- [16] Flory Wong and Ayusman Sen. Progress toward Light-Harvesting Self-Electrophoretic Motors: Highly Efficient Bimetallic Nanomotors and Micropumps in Halogen Media. *ACS Nano*, 10(7):7172–7179, July 2016. Publisher: American Chemical Society.
- [17] Xi Chen, Xiaowen Chen, Mohamed Elsayed, Harrison Edwards, Jiayu Liu, Yixin Peng, H. P. Zhang, Shuailong Zhang, Wei Wang, and Aaron R. Wheeler. Steering Micromotors via Reprogrammable Optoelectronic Paths. *ACS Nano*, March 2023. Publisher: American Chemical Society.
- [18] Yang Wang, Rose M. Hernandez, David J. Bartlett, Julia M. Bingham, Timothy R. Kline, Ayusman Sen, and Thomas E. Mallouk. Bipolar Electrochemical Mechanism for the Propulsion of Catalytic Nanomotors in Hydrogen Peroxide Solutions. *Langmuir*, 22(25):10451–10456, December 2006. Publisher: American Chemical Society.
- [19] Alyosha Christopher Molnar, Sunwoo Lee, Alejandro Cortese, Paul McEuen, Sanaz Sadeghi, and Shahaboddin Ghajari. Nanoliter-Scale Autonomous Electronics: Advances, Challenges, and Opportunities. In *2021 IEEE Custom Integrated Circuits Conference (CICC)*, pages 1–6, April 2021. ISSN: 2152-3630.
- [20] Ryan St. Pierre and Sarah Bergbreiter. Toward Autonomy in Sub-Gram Terrestrial Robots. *Annual Review of Control, Robotics, and Autonomous*

- Systems*, 2(1):231–252, 2019. eprint: <https://doi.org/10.1146/annurev-control-053018-023814>.
- [21] Seokhyeon Jeong, Zhiyoong Foo, Yoonmyung Lee, Jae-Yoon Sim, David Blaauw, and Dennis Sylvester. A Fully-Integrated 71 nW CMOS Temperature Sensor for Low Power Wireless Sensor Nodes. *IEEE Journal of Solid-State Circuits*, 49(8):1682–1693, August 2014. Conference Name: IEEE Journal of Solid-State Circuits.
- [22] Alejandro J. Cortese, Conrad L. Smart, Tianyu Wang, Michael F. Reynolds, Samantha L. Norris, Yanxin Ji, Sunwoo Lee, Aaron Mok, Chunyan Wu, Fei Xia, Nathan I. Ellis, Alyosha C. Molnar, Chris Xu, and Paul L. McEuen. Microscopic sensors using optical wireless integrated circuits. *Proceedings of the National Academy of Sciences*, 117(17):9173–9179, April 2020. Publisher: Proceedings of the National Academy of Sciences.
- [23] Francarl Galea, Owen Casha, Ivan Grech, Edward Gatt, and Joseph Micallef. Ultra Low Frequency Low Power CMOS Oscillators for MPPT and Switch Mode Power Supplies. *2018 14th Conference on Ph.D. Research in Microelectronics and Electronics (PRIME)*, pages 121–124, July 2018. Conference Name: 2018 14th Conference on Ph.D. Research in Microelectronics and Electronics (PRIME) ISBN: 9781538653876 Place: Prague Publisher: IEEE.
- [24] Usama Zaghoul and Gianluca Piazza. 10–25 NM piezoelectric nano-actuators and NEMS switches for millivolt computational logic. In *2013 IEEE 26th International Conference on Micro Electro Mechanical Systems (MEMS)*, pages 233–236, January 2013. ISSN: 1084-6999.
- [25] G. Tuin, J. H. J. E. Senders, and H. N. Stein. Electrophoretic Properties of Monodisperse Polystyrene Particles. *Journal of Colloid and Interface Science*, 179(2):522–531, May 1996.
- [26] L. E. Ermakova, N. F. Bogdanova, and M. P. Sidorova. Effect of the Surface Pretreatment on the Electrokinetic Properties of Silicon and Silicon Oxide. *Colloid Journal*, 65(4):428–433, July 2003.
- [27] Walter F. Paxton, Shakuntala Sundararajan, Thomas E. Mallouk, and Ayusman Sen. Chemical Locomotion. *Angewandte Chemie International Edition*, 45(33):5420–5429, 2006. eprint: <https://onlinelibrary.wiley.com/doi/pdf/10.1002/anie.200600060>.
- [28] Walter F. Paxton, Ayusman Sen, and Thomas E. Mallouk. Motility of Catalytic Nanoparticles through Self-Generated Forces. *Chemistry – A European Journal*, 11(22):6462–6470, November 2005. Publisher: John Wiley & Sons, Ltd.

- [29] Nicola Pellicciotta, Ojus Satish Bagal, Viridiana Carmona Sosa, Giacomo Frangipane, Gaszton Vizsnyiczai, and Roberto Di Leonardo. Light Controlled Biohybrid Microbots. *Advanced Functional Materials*, 33(39):2214801, 2023. [_eprint: https://onlinelibrary.wiley.com/doi/pdf/10.1002/adfm.202214801](https://onlinelibrary.wiley.com/doi/pdf/10.1002/adfm.202214801).
- [30] Gregory Dudek and Michael Jenkin. *Computational Principles of Mobile Robotics*. Cambridge University Press, 2 edition, July 2010.
- [31] Gene F. Franklin, J. David Powell, and Abbas Emami-Naeini. *Feedback control of dynamic systems*. Pearson, Upper Saddle River [N.J.], 6th ed edition, 2010. OCLC: ocn316017520.
- [32] Kevin M. Lynch and Frank C. Park. *Modern robotics: mechanics, planning, and control*. Cambridge university press, Cambridge, 2017.
- [33] Xiaopu Wang, Chengzhi Hu, Lukas Schurz, Carmela De Marco, Xiangzhong Chen, Salvador Pané, and Bradley J. Nelson. Surface-Chemistry-Mediated Control of Individual Magnetic Helical Microswimmers in a Swarm. *ACS Nano*, 12(6):6210–6217, June 2018. Publisher: American Chemical Society.
- [34] Gwangjun Go, Hyunchul Choi, Semi Jeong, Seong Young Ko, Jong-Oh Park, and Sukho Park. Selective microrobot control using a thermally responsive microclammer for microparticle manipulation. *Smart Materials and Structures*, 25(3):035004, February 2016. Publisher: IOP Publishing.
- [35] Chytra Pawashe, Steven Floyd, and Metin Sitti. Multiple magnetic microrobot control using electrostatic anchoring. *Applied Physics Letters*, 94(16):164108, April 2009.
- [36] Eric Diller, Joshua Giltinan, and Metin Sitti. Independent control of multiple magnetic microrobots in three dimensions. *The International Journal of Robotics Research*, 32(5):614–631, April 2013. Publisher: SAGE Publications Ltd STM.
- [37] Daniel Ahmed, Mengqian Lu, Amir Nourhani, Paul E. Lammert, Zak Stratton, Hari S. Muddana, Vincent H. Crespi, and Tony Jun Huang. Selectively manipulable acoustic-powered microswimmers. *Scientific Reports*, 5(1):9744, May 2015.
- [38] Sumit Mohanty, Qianru Jin, Guilherme Phillips Furtado, Arijit Ghosh, Gayatri Pahapale, Islam S. M. Khalil, David H. Gracias, and Sarthak Misra. Bidirectional Propulsion of Arc-Shaped Microswimmers Driven by Precessing Magnetic Fields. *Advanced Intelligent Systems*, 2(9):2000064, 2020. [_eprint: https://onlinelibrary.wiley.com/doi/pdf/10.1002/aisy.202000064](https://onlinelibrary.wiley.com/doi/pdf/10.1002/aisy.202000064).

- [39] Tomasz Kozacki and Maksymilian Chlipala. Color holographic display with white light LED source and single phase only SLM. *Optics Express*, 24(3):2189–2199, February 2016. Publisher: Optica Publishing Group.
- [40] Xinghao Hu, Immihan C. Yasa, Ziyu Ren, Sandhya R. Goudu, Hakan Ceylan, Wenqi Hu, and Metin Sitti. Magnetic soft micromachines made of linked microactuator networks. *Science Advances*, 7(23):eabe8436, June 2021. Publisher: American Association for the Advancement of Science.
- [41] Qingkun Liu, Wei Wang, Michael F. Reynolds, Michael C. Cao, Marc Z. Miskin, Tomas A. Arias, David A. Muller, Paul L. McEuen, and Itai Cohen. Micrometer-sized electrically programmable shape-memory actuators for low-power microrobotics. *Science Robotics*, 6(52):eabe6663, March 2021. Publisher: American Association for the Advancement of Science.
- [42] Li Xu, Maya Lassiter, Xiao Wu, Yejoong Kim, Jungho Lee, Makoto Yasuda, Masaru Kawaminami, Marc Miskin, David Blaauw, and Dennis Sylvester. A 210x340x50um Integrated CMOS System for Micro-Robots with Energy Harvesting, Sensing, Processing, Communication and Actuation. In *2022 IEEE International Solid-State Circuits Conference (ISSCC)*, volume 65, pages 1–3, February 2022. ISSN: 2376-8606.

1 Figures

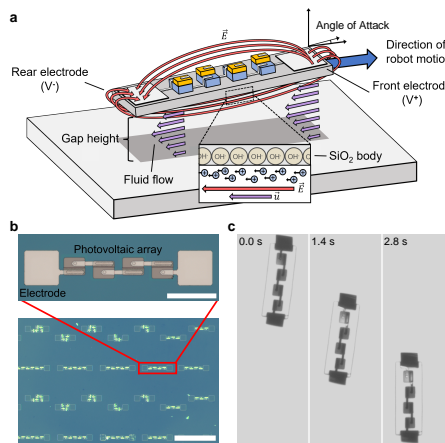


Fig. 1 Electrokinetic propulsion for microrobots (a), Schematic of the electrokinetic mechanism. Positively charged ions in the electrical double layer migrate in the presence of an electric field, \vec{E} , and generate fluid flows around the device that cause locomotion. **(b)**, Micrograph of a 4 PV design with Ti/Pt electrodes at both ends of the device's SiO₂ body (scale bar 100 μm). Beneath it, a micrograph of various robot designs on chip, fabricated massively in parallel with 400 devices per 1.5 cm square chip (scale bar 500 μm). **(c)**, Timelapse of a device locomoting under global microscope illumination in 5 mM hydrogen peroxide.

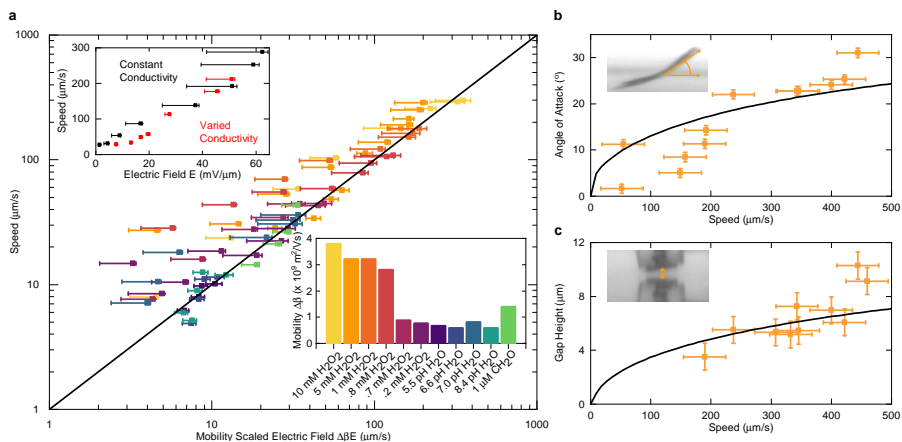


Fig. 2 Characterization of propulsion mechanism (a), The upper inset shows the speed vs electric field data for a robot in 5 mM hydrogen peroxide, where the electric field strength is estimated as the quotient of current density and solution conductivity adjusted by a scale factor set by the geometry of the robot (see Methods). The main data are the speed vs electric field behavior for a variety of solutions scaled by the robot's effective mobility $\Delta\beta$, which is determined by linear fitting of the raw speed vs electric field data for each solution (see Methods). The black line is unity. The lower inset details the variation of the effective mobility for different solution compositions. The electric field error bars are the propagated measurement uncertainties of current and conductivity, where the negative skew in these errors is a due to the larger uncertainty associated with solution contamination, which can only cause conductivity to increase. **(b),(c)**, Data for the angle of attack and gap height vs speed, respectively, for a robot in 5 mM hydrogen peroxide. The black curves are the results of numerical fitting of the data to our fluid model (see Methods). The insets show micrographs of a moving robot viewed from the side and front, from which we measured the angle and gap height. The error bars are uncertainty estimates set by the resolution of the cameras (see Methods).

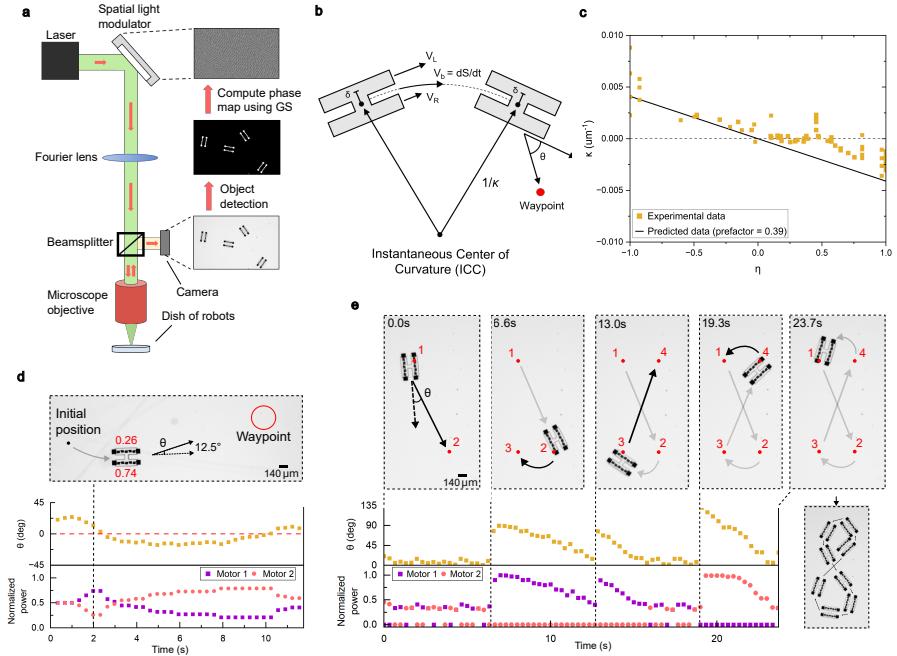


Fig. 3 Optical control and kinematics of a two engine robot (a), The closed-loop optical system that allows for automated control over robots in the microscope FOV. After each frame capture, the computer performs object detection, generates a new optical pattern using the Gerchberg-Saxton (GS) algorithm, and updates the spatial light modulator to shoot light at the newly detected robot positions. **(b)**, A two-motor robot traveling to a waypoint has a body velocity of V_b with engine separation 2δ . Robots travel along arcs of curvature κ . The misalignment angle θ is the angle between the robot's heading and the vector that points from the robot's center of mass to the target position. **(c)**, Values of curvature κ extracted from multiple experiments show the robot's turning behavior linearly depends on the normalized difference between engine velocities η . The black line gives predicted values of curvature for a differential drive robot with an additional prefactor of 0.39 to account for optical effects (see Methods). **(d)**, Implementation of a standard differential drive controller. Both motors are powered simultaneously and the power in each is trimmed in order to obtain propulsion towards the waypoint with a low misalignment angle ($\theta < 15^\circ$). See Supplemental Video 4. **(e)**, Path trace of a proportional controller capable of directing the robot to a series of waypoints by powering the left or right motor with a value weighted by the misalignment angle θ . If the misalignment angle is less than a user-defined threshold (here 7.5°) for consecutive frames, both motors get the same power simultaneously. See Supplemental Video 5.

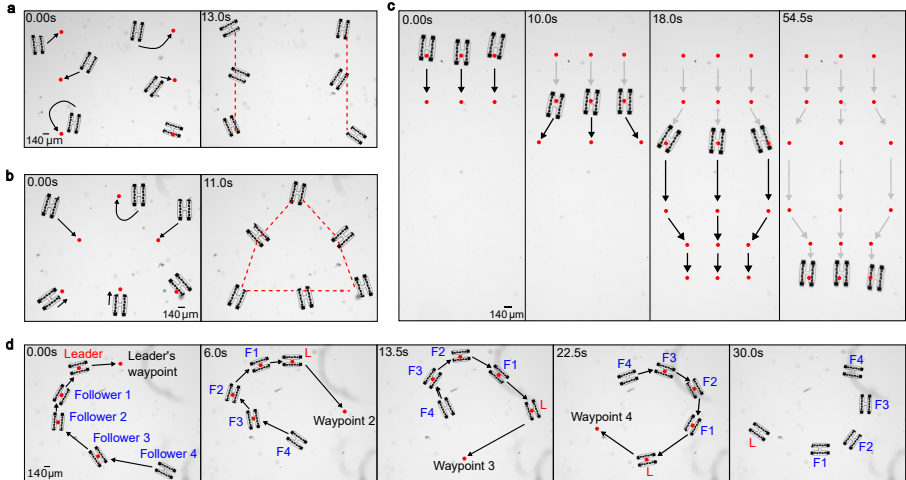


Fig. 4 Addressability and swarming behavior (a),(b), The control program can be given a single list of target positions in order to rearrange the robots based on their nearest waypoint. **(c)**, Robots can be assigned individual lists of waypoints in order to trace out separate paths in unison. **(d)**, Waypoints can also be dynamic and change at each timestep. Shown in blue, “follower” robots are assigned the location of another robot in the system as a waypoint. This rule results in chain-like structures following the “leader”, shown in red.

2 Methods

Microrobot fabrication. For our fabrication process (see Extended Data Fig. E3), we use silicon-on-insulator wafers from Ultrasil corporation with a 2 μm device layer (p-type doped, 0.1 Ohm-cm), 500 nm silicon dioxide layer, and 500 μm silicon handle thickness. 15 mm chips are diced from a 4 inch wafer using a dicing saw, spin coated with P509 spin-on glass from Filmtronics, and postbaked for 20 minutes at 120°C. We use a rapid thermal annealer to diffuse the P509 (n-type phosphorus) dopants by annealing for 30 minutes at 800°C in an N_2 environment to form a layer of n-type silicon above the p-type silicon. Once the doping is complete, we remove the spin-on glass by immersing the chip in 6:1 buffered oxide etch (BOE).

We build the photovoltaics (PVs) through a series of etching and metalization steps. Before starting, we measure the thickness of the silicon device layer precisely at four different locations across the sample using a Filmetrics reflectometer. We spin on Shipley 1813 photoresist and expose using a mask aligner. Next, we develop the exposed photoresist in AZ300 MIF developer for 50 seconds and O_2 plasma clean the sample at 150 W for 90 seconds. We etch in an RF plasma SF_6/O_2 environment for 40 seconds to expose the p-type device layer silicon and then measure the thickness of the silicon again to confirm an etch depth of at least 1 μm . We strip the photoresist by ultrasonically cleaning in heated PG remover for 10 minutes and O_2 plasma cleaning at 150 W for 90 seconds.

Our second etch step forms discrete PVs. First, we spin on an HMD-S/AZ3330 photoresist stack and expose using a mask aligner. Next, we develop the exposed photoresist in AZ300 MIF developer for 50 seconds and O₂ plasma clean at 150 W for 90 seconds. We adhere our samples to a carrier wafer using CrystalBond and perform an anisotropic Bosch etch with a deep reactive ion etcher. Using the insulating oxide layer of the SOI as an etch stop, we completely clear away the device layer silicon in the exposed regions to form discrete PV cells. We remove the samples from the carrier wafer by ultrasonically in heated (70°F) water and then strip the photoresist by ultrasonically in heated PG remover for 10 minutes. We then O₂ plasma clean the samples at 150 W for 90 seconds.

Next, we make metal contacts on the p-type and n-type silicon. We start by insulating the PVs by depositing a 20 nm conformal layer of silicon dioxide using an atomic layer deposition (ALD) tool. We spin on HMDS/AZ3330 photoresist, expose in a mask aligner, and develop in AZ300 MIF developer for 50 seconds to form small openings in the photoresist to the p-type and n-type silicon. We O₂ plasma clean at 150 W for 90 seconds then immerse the samples in 6:1 BOE for 15 seconds to remove the insulating oxide layer in the exposed regions. Before the native oxide layer regrows on the exposed silicon, we sputter 20 nm of titanium and 40 nm of platinum over the entire sample. We then perform a lift-off by stripping the AZ3330 photoresist in heated PG remover with ultrasonication, followed by an O₂ plasma clean at 150 W for 90 seconds. Finally, we anneal the contacts in a rapid thermal annealer for 5 minutes at 400°C in an N₂ environment.

To wire the PVs together and form the device's electrodes, we spin on HMDS/AZ3330 photoresist, expose in a mask aligner, develop in AZ300 MIF developer for 50 seconds, and O₂ plasma clean at 150 W for 90 seconds. We sputter 20 nm of titanium followed by 40 nm of platinum and perform a liftoff process in heated PG remover with ultrasonication to form interconnects between the PVs and electrodes at either end of the PV line.

Next, we define the shape of the robot's body by etching the silicon dioxide layer of the SOI in the regions between robots. We spin on HMDS/AZ3330, expose in a mask aligner, and develop in AZ300 MIF for 50 seconds. We O₂ plasma clean at 150W for 90 seconds and perform a 25 minute CF₄ etch to remove the exposed silicon dioxide. We then verify that the oxide has been removed using a Filmetrics reflectometer and strip the photoresist in heated PG remover with ultrasonication.

In order to insulate our electronics stack from the surrounding solution, we spin coat SU-8 2005 epoxy at 3000 RPM for 30 seconds with a 1000 RPM/s ramp rate. We soft bake the samples at 65°C for 1 minute and then at 90°C for 2 minutes before stripping the edge bead and exposing in a mask aligner through an I-line filter. After the sample is exposed, we bake the chips at 65°C for 1 minute, transfer to a separate hotplate to bake at 95°C for 3 minutes, develop for 60 seconds in SU-8 developer with agitation, followed by a rinse in IPA. We then hard bake the SU-8 at 65°C for 1 minute, transferring the

samples to a 95°C hot plate, and ramping up to 150°C where the samples are held for 5 minutes. Subsequently, we turn off the hot plate and allow the sample to cool to room temperature to relieve thermal stress in the epoxy. We O₂ plasma clean at 150 W for 90 seconds.

We then sputter 200 nm of aluminum, followed by 10 nm of alumina deposited via ALD. We spin on an HMDS/AZ3330 stack, expose in a mask aligner, and develop in AZ300 MIF for 120 seconds with constant agitation to form small openings to the alumina/aluminum around the perimeter of the robots. After an O₂ plasma clean at 150 W for 90 seconds, we post-bake the samples at 115°C for 2 minutes and place them in aluminum etchant A for at least 20 minutes to clear the alumina/aluminum stack and expose the handle silicon. We remove the photoresist and run a XeF₂ etch to remove the underlying silicon through the holes patterned in the aluminum and suspend the devices in air. Lastly, we etch away the alumina/aluminum stack holding the devices by placing the samples in 10:1 diluted aluminum etchant A overnight. Once the aluminum is removed, we pipette the free floating devices out of the etchant and into deionized water for storage.

Characterizing PVs. PVs were characterized by probing with tungsten microprobes (Signatone SM-35) and performing current-voltage sweeps at various illumination intensities using a Keithley source meter (2450). Individual PVs output photocurrents on the order of 100 nA and open circuit voltages of approximately 500 mV when illuminated with a white light source (Thorlabs Solis 1-D) at maximum power in an upright microscope (Olympus) (Extended Data Fig. E4). Open circuit voltages sum for multiple PVs wired in series, enabling the devices to operate effectively as current sources in solution (Extended Data Fig. E5).

Solution and substrate preparation. Hydrogen peroxide solutions were prepared by dilution of 30% hydrogen peroxide (Fisher H325-500) with DI water from our facility with an initial conductivity of 250 nS/cm. Conductivity of solutions was adjusted with addition of sodium nitrate (Sigma-Aldrich S5506-250G) and sodium nitrite (Fisher S347-500) at various concentrations. Buffer solutions were prepared by dilution of various buffers (Fisher SB107-500, Fisher SB115-500, Fisher SB101-500), and 50% sodium hydroxide (Transene 1310-73-2). Formaldehyde solutions were prepared by dilution of 37% formaldehyde stabilized with methanol (Fisher F79-500). Solution pH was measured with a Hach Pocket Pro pH meter (PN 9531000) and solution conductivity was measured with a Hannah Instruments pure water conductivity meter (HI98197). Polystyrene substrates used were sterile 60 x 15 mm petri dishes (VWR International 25384-D92). Glass substrates used were microscope slides (Fisher 12-549-3 and Thorlabs MS10PC1, for negative and positive surface functionalization respectively). Platinum substrates used were made by sputtering 20 nm of titanium and 40 nm of platinum on a 25 mm glass cover slip (Deckglaser 100). SU-8 substrates and microfluidic channels used were made by spinning SU-8 2050 photoresist on a 4 inch borofloat wafer at 2000 rpm for 40 seconds, soft baking 9 minutes at 95°C, exposing regions around channels

with a mask aligner through an I-line filter, post baking for 7 minutes at 95°C, developing in SU-8 developer for 7 minutes with agitation, rinsing with IPA, and hard baking for 5 minutes at 200°C.

Measuring the speed vs. current response of a single motor robot.

To measure the current driven through solution by a robot under various illumination intensities we fabricate two test chips: a test chip with PV circuits identical to those on the robots, and a test chip with identical electrodes. The electrode test chip is immersed in the desired solution under a stereoscope (ZEISS SteREO Discovery.V8), and the PV test chip is placed under an upright optical microscope in air (Olympus). We probe the circuits on the PV chip with tungsten probes (Signatone SM-35) under illumination in reflection mode with a variable intensity white LED source (Thorlabs Solis-1D). We probe the electrodes on the electrode chip with insulated Pt/Ir probes (Microprobes for Life Science PI20031.5A5). We then wire the probes from each chip in series, such that the PV circuit is driving current through the electrodes in solution, which we measure at various light intensities with a low noise current preamplifier (Stanford Research Systems SR570). The results of these measurements are detailed in Extended Data Figure E6. We then place a single motor robot in the same solution used to measure the current, and illuminate the robot at the same light intensities in order to measure the speed. We take 10 frame per second image sequences of the robot in motion and compute the center of mass of the robot in each frame through image thresholding and particle detection (ImageJ). The position data is smoothed by convolution with a Gaussian kernel, and the instantaneous speed is calculated for each frame as the magnitude of the position change divided by the time between frames. The reported speed is the average of all instantaneous speeds for the duration of the experiment, usually a few seconds.

Estimating field strength and mobility coefficient. The magnitude of the field in the solution at the electrode interfaces can be computed simply as $J/\sigma = I/a^2\sigma$, where I is the current generated by the PVs, a is the side length of each electrode, and σ is the solution conductivity. However, since the pressures and shears that drive propulsion occur in the fluid gap underneath the robot, we seek to estimate the field strength due to current flowing in this region. This can be achieved by first estimating the voltage drop in the solution between the electrodes. For the simple case of a 2D electrode on an insulating substrate with characteristic size a and current density J , the potential at the electrode interface relative to a point at infinity can be found from the Laplace equation to be $\Delta\phi \sim I/a\sigma$. By the linearity of solutions to the Laplace equation, this result holds for the case where a grounding electrode of the same size lies at some lateral distance l from the first electrode, yielding an expression for the potential drop between them. We can thus approximate the field magnitude as $E \sim \Delta\phi/l = I/a\sigma l = Ja/\sigma l$. In other words, the propulsive field strength is equal to the field magnitude at the electrode interface reduced by a factor a/l . To estimate the mobility coefficient for each solution the speed vs field graphs are fit via linear regression, with the speed at zero

field constrained to be zero. The data in Figure 2a are scaled by the effective mobility to force data collapse.

Measuring angle of attack and gap height. To measure angle of attack and gap height, a two motor robot is placed on a piece of polystyrene in a glass cuvette (Thorlabs CV10Q35A), and imaged simultaneously from the side using an adjustable magnification microscope (Olympus) in transmission mode, and from above using a stereoscope (ZEISS SteREO Discovery.V8), while illuminated at various intensities with a ring light (Schott S80-55). The speed of the device is measured using image sequences from the stereoscope, and the angle of attack and gap height are measured using image sequences from the side mounted microscope.

Modeling Microrobot Propulsion. From the side imaging of robots, we observe that the fluid gap underneath the robot is significantly smaller than the robot's length, l or width, w . This allows for a considerable simplification of both the electrical and fluid parts of the problem by focusing on the field and flows within the gap, as these should dominate the overall behavior of the system.

We approximate the gap profile as a linear function along the direction of transit (here the x-axis) and as a constant along the orthogonal axis (the y-axis, defining the robot's width). The z-axis points along the gap direction. A schematic of our coordinate system is included as Extended Data Figure E7.

In the electrical domain, we assume electrical current flowing across the robot's body is governed by Ohm's law $\nabla^2\phi = 0$. Since there is a no flux boundary for current both at the lower substrate and the robot's body, we expect current flow along the z-axis (i.e. along the gap direction) to be negligible. Thus, we integrate the potential from the top to the bottom of the gap, reducing the electric field equation to

$$\partial_x(h(x)\partial_x\phi) + \partial_y(h(x)\partial_y\phi) = 0 \quad (1)$$

Ignoring field variations across the robot's width (y-axis), as no bias is applied along this direction, we find the field is approximately governed by

$$\partial_x(h(x)\partial_x\phi) = 0 \quad (2)$$

Enforcing that the potential equals the applied electrode potential at either end of the robot leads to the solution

$$\phi(x) = (\Delta\phi)\left[\frac{\log[h(x)]}{\log[h_+/h_-]} - \frac{(h_+ + h_-)}{2\alpha} \log\left[\frac{h_+ + h_-}{2}\right]\right] \quad (3)$$

where h_+ is the largest height of the gap, h_- is the lowest and $(\Delta\phi)$ is the applied potential drop. We note the first term conveys all the relevant physics since it is the only part of the expression with spatial dependence and the field alone contributes to propulsion. The second term is simply a reference

potential chosen so that in the limit $\alpha \rightarrow 0$ the potential is approximately $\phi(x) \approx (\Delta\phi)x/l$.

Turning to the fluid domain, forces on the robot are computed by contracting the fluid stress tensor, $\sigma_{ij} = -p(x)\delta_{ij} + \mu(\partial_i u_j + \partial_j u_i)$, with the normal vector on the robot's body, $\hat{n} = \alpha/\sqrt{1 + \alpha^2}\hat{x} - 1/\sqrt{1 + \alpha^2}\hat{z}$. Here p is the pressure, u_i is the velocity of the fluid flow in the i th direction, and μ is the fluid viscosity. In the lubrication approximation, we assume that p is independent of z , that the dominate viscous stress term is $\partial_z u_x$, and that the fluid velocity along the x direction is given by $u_x = \frac{1}{2\mu}\partial_x p(z^2 - zh(x)) + (V + \Delta\beta E_x)z/h + \beta_- E_x$, where $\Delta\beta$ is the difference in surface slip coefficients, β_- is the slip coefficient of the surface under the robot, and $E_x = -\partial_x \phi(x)$. The resulting lift, drag and torque equations respectively read [43–45]

$$f_z = \langle p \rangle + \mu\alpha\langle (V + \Delta\beta E_x)/h(x) \rangle \quad (4)$$

$$f_x = \frac{\alpha}{2}\langle p \rangle + \mu\langle (V + \Delta\beta E_x)/h(x) \rangle \quad (5)$$

$$\tau = \langle xp \rangle + \mu\alpha\langle (V + \Delta\beta E_x)x/h(x) \rangle \quad (6)$$

where angle brackets denote integration over the robot's area $\langle p \rangle = \int_{-l/2}^{l/2} dx \int_{-w/2}^{w/2} dyp$. The right hand sides represent forces from the lubrication zone, whereas the left hand side represents any external forcing.

Solving the fluid forces requires computing the pressure under the robot. Within the lubrication approximation, the pressure satisfies the Reynolds equation [43–45]:

$$\frac{1}{12\mu}\partial_i(h^3\partial_i p) = \frac{1}{2}\partial_i(h(u_i^+ + u_i^-)) + u_z^+ - u_z^- - u_i^+\partial_i h \quad (7)$$

where u_i^+ represents a fluid velocity in the i th direction on the upper surface, u_i^- denotes fluid velocities on the lower surface and contracted indices sum only on the x and y directions (i.e. the pressure is a function only of x and y).

To simplify the calculation, we exploit the linearity of low Reynolds number flow and split the pressure into two contributions: one from the translations and rotations of the robot's body (p_m) and the other from the electric field induced boundary slips (p_{ek}). These different boundary conditions for the fluid each set different terms on the right hand side of equation 7.

For the flow from rotation and translation, the boundary conditions simplify considerably. Here all lower surface velocities $u_i^- = 0$ while on the upper surface, there is motion from rigid translation in the x and z directions and a spatially varying velocity due to rotation around the center of mass. Specifically, $u_x^+ = V$ and $u_z^+ = U + x\dot{\alpha}/(1 + \alpha^2)$. Inserting these expressions gives the equation for the rotation/translation part of the pressure [43, 44]

$$\frac{1}{12\mu}\partial_i(h^3\partial_i p_m) + V\alpha/2 = (U + x\dot{\alpha}/(1 + \alpha^2)) \quad (8)$$

As a boundary condition, pressure is assumed to vanish anywhere outside the surface of the robot, as there is no surface here to support stresses.

For the electrokinetic contribution to the pressure, all the fluid velocities at interfaces are proportional to the electrokinetic slip. Thus $u_i^+ = \beta^+ E_i$ and $u_i^- = \beta^- E_i$. The resulting Reynolds equation for this part of the flow is:

$$\frac{1}{12\mu}\partial_i(h^3\partial_i p_{ek}) = \partial_i(h(\beta^+ + \beta^-)E_i)/2 + \beta^+ E_z(z = h) - \beta^+ \alpha E_x(z = h) \quad (9)$$

We find all the terms on the right hand side cancel identically. First, we note that the last two terms on the right hand side cancel, since the no-flux condition on the electric field through the robot's body implies $\hat{n} \cdot \vec{E} \propto E_x \alpha - E_z = 0$. Likewise, the first term on the right hand side is zero via equation 1. Without source terms, the boundary condition of vanishing pressure outside the robot's body means the electrokinetic portion of the flow does not contribute to pressure and its sole forcing is through shear stress.

Since we are not interested in the pressure itself, but rather its integral over the robot's surface, we can numerically compute the forces and torques in equation 4 using the variational approach in [44, 45]. Specifically, equation 8 implies the pressure also minimizes the functional

$$\langle [\frac{\partial_i p h^3 \partial_i p}{12\mu} - p(V\alpha/2 - U - \dot{\alpha}x/(1 + \alpha^2))] \rangle \quad (10)$$

Thus, we approximate $p \approx (y^2 - (w/2)^2) \sum_{n=1}^N \sin[n\pi(x + l/2)/l] a_n$ where a_n are free parameters chosen to minimize equation 10. This expansion takes the first two terms of a Taylor series in the y coordinate, accounting for symmetry and boundary conditions, and expands pressure variation along the x-axis in terms of trigonometric functions that vanish at the ends of the robot. Inserting this form into equation 10 and minimizing reduces finding the pressure to a sparse linear algebra problem, which is efficient to solve numerically.

For the external forcing in equation 4, we assume $f_z = mg$ and introduce two phenomenological parameters $\tau = a\Delta\phi$ and $f_x = b\Delta\phi$. These parameters are motivated by additional experiments in which robots on their sides were observed to translate and rotate in proportion to the incident optical power.

To find the robot's equilibrium state, we insert the pressure expansion and external force parameters a into equation 4 with the optimal a_n . The three equations can be used to solve for the velocity in terms of the field and forcing parameters alone. This result can be reinserted into equation 4 to give two closed equations for the gap height and angle of attack evolution. We solve

these two equations numerically (using Scipy’s ODEInt Package) until they reach equilibrium to find the steady state speed, angle of attack, and velocity.

To produce the fits in Figure 2b and c, we used the Nelder-Meade simplex algorithm to simultaneously minimize the mean square error between the observed data and numerical solutions. Data and the the model were written in dimensionless form, scaling all lengths by the robot’s longest dimension l , all velocities by the viscous settling time $\mu l/mg$, and all forces by mg . The resulting system of equations has three free parameters: the scaling between velocity and electric field and the phenomenological torque and shear parameters a and b , which the solver adjusts to minimize error.

All of the code used for solving for the pressure, integrating the ODE and fitting the data is included in the supplementary material.

Forming computer generated holograms. To form optical patterns in the microscope field of view, we mimic setups that are capable of reconstructing 2D or 3D holograms by displaying grayscale phase maps on an SLM [39, 46, 47]. Using a Holoeye LETO-3 SLM in a phase-modulation scheme, we run the Gerchberg-Saxton (GS) algorithm on a grayscale image containing the optical pattern we want to create [48]. This algorithm extracts a phase map that will diffractively reconstruct the target optical pattern in the far-field plane of the microscope after passing through a lens [49, 50]. Additionally, to handle swapping between the coordinate system of the microscope FOV (5320 x 3032 pixels) and the SLM display (1920 x 1080 pixels), we generate an affine transformation matrix using an automated calibration program. This program places non-collinear points with known (x, y) coordinates on the SLM, detects the corresponding (x', y') points in the microscope FOV, and generates a transformation matrix to map $(x, y) \leftrightarrow (x', y')$. At each time step, we apply this matrix to the output of the GS algorithm to generate a phase map for the SLM that recreates the desired optical pattern in the microscope FOV with the correct scale, rotation, and shear. Further, as shown in in Figure 3a, the SLM is tilted at an angle relative to the incident laser light. This skew steers the 0th order spot, which cannot be modulated by the SLM, off the center of the optical axis. We then apply a blazed grating to the phase map extracted by the GS algorithm to bring the 1st order diffraction pattern back to the center of the optical axis and into the backplane of the microscope [51].

Model for predicting κ . As seen in Figure 3a, in an ideal differential drive system lateral motion is prohibited and the path of the robot can be described by its progression along a tangent circle with curvature κ . The robot travels with a body velocity V_b and the motor separation is given by 2δ . We write the following equations for the left and right motor velocities:

$$V_L = V_b(1 + \delta\kappa) \tag{11}$$

$$V_R = V_b(1 - \delta\kappa) \tag{12}$$

The body velocity V_b can be written as $\frac{V_L}{2} + \frac{V_R}{2}$. We solve for the curvature κ by subtracting V_L and V_R using this substitution for V_b .

$$\kappa = \frac{V_L - V_R}{(V_L + V_R)\delta} \quad (13)$$

We previously defined $\eta = (V_L - V_R)/(V_L + V_R)$, so we write κ as:

$$\kappa = \frac{\eta}{\delta} \quad (14)$$

While Equation 14 describes an ideal differential drive system, we find empirically that the direct relationship between light intensity and motor velocity requires an additional term to capture the effect of optical power incident on one motor spilling over to the other motor due to imperfect hologram resolution. We extract this term experimentally by measuring the speed of a motor when the optical power is incident on the motor and again when it the laser spot is offset by a distance δ . The ratio of these two values gives the adjustment prefactor. Experimentally we find a value of 0.39 for the devices shown in Figure 3 and Figure 4. To find the predicted values of curvature seen in Figure 3c we calculate Equation 14 for the entire range of η and multiply by this prefactor.

Control laws. We implement two controllers in Figure 3d and Figure 3e. In both demonstrations, the computer calculates a misalignment angle θ after every frame capture as the angle between the robot’s heading and a vector that points from the robot’s center of mass to the target position. In the first control scheme, if θ is increasing or larger than a user-defined threshold (here 15°), the controller increases the power on the motor farther from the waypoint to realign the robot. If θ is decreasing, the power proportion is not changed. Using this rule, the controller maintains a misalignment angle of less than 15° over a majority of the path trace (Fig. 3d). With the same definition of θ , the second controller is a proportional controller that directs the robot by powering the left motor, the right motor, or both when θ is smaller than a user-defined threshold (here 7.5°) for two consecutive frames. Additionally, this controller uses θ to weight the motor power. As seen in Figure 3e, sharp increases in θ after receiving a new waypoint results in the controller sending all available power to a single motor for turning.

Scaling up to more robots. While this work represents a first-pass attempt to demonstrate the capabilities of this platform, we have a direct route towards scaling this system up to an order of magnitude more devices. For example, given a two-motor robot of size $400 \times 305 \mu\text{m}$, a swarm of 500 devices can fit in an area of $8 \times 8 \text{ mm}^2$. Our LETO-3 SLM has a pixel pitch of $6.4 \mu\text{m}$ and an active area of $12.29 \times 6.91 \text{ mm}^2$, meaning that we could pattern light with sub $10 \mu\text{m}$ precision over the entire area of the swarm to accomplish the level of control seen in Figure 3 and Figure 4. The associated increase in power

demand can be met by increasing the laser power illuminating the SLM or by staggering robot activation as needed. To avoid increased crosstalk between nearby devices additional optical elements, such as polarizers, can be used to reduce optical ghosting and increase hologram resolution.

Notably, the computation requirements do not significantly change when the system size increases, as the runtime of the closed-loop control system is dominated by two, scale-independent steps: Extraction of the phase map with the GS algorithm and updating the SLM display with a new optical pattern. The first has a leading order time-complexity of $\mathcal{O}(N^2 \log(N^2))$ set by the Fourier transform steps of the GS algorithm and is shown to have a convergence time dependent on the size of the target image. By maintaining a target image resolution of 1920 x 1080 pixels, we can increase the complexity of the optical pattern to control more devices without sacrificing computation time [52]. The runtime of the second step is set by the bus speed and switching speed of the SLM and does not depend on image complexity, image resolution, or the number of devices in the system.

We emphasize that the scalability and control of this system stems from using light. Other works such as opto-thermoelectric microswimmers [53], biohybrid micromotors powered by light [29], and micromotors steered by optoelectronic paths [17] also demonstrate the promise and ease of using patterned light for control. In contrast, non-optical control schemes are successful in performing tasks such as traveling to a target location, but are harder to scale as they rely on magnetic fields, ultrasound signals, or chemical reactions which are difficult to multiplex. For example, arc-shaped microswimmers driven by varying precessions of magnetic field show different propulsion modes based on the tilt angle of the robot's head, but require fabrication differences between individual robots for selective control [38]. Robots containing microbubbles are steered by a combination of magnetic fields and ultrasound signals, but selective control requires engineering different bubble sizes within the robot body [37]. Further, independent propulsion of 4 helical microswimmers is shown but requires different surface chemistry on each robot [33]. Using light requires no fabrication differences between robots and is simple to multiplex for selective control with SLMs or digital micromirror devices.

References

- [43] L. Gary Leal. *Advanced transport phenomena: fluid mechanics and convective transport processes*. Cambridge University Press, Cambridge, 2007. OCLC: 173817039.
- [44] A. Z. Szeri. *Fluid film lubrication*. Cambridge University Press, Cambridge, U.K., 2nd ed edition, 2011. OCLC: 719369575.
- [45] A. Szeri and D. Powers. Pivoted Plane Pad Bearings: A Variational Solution. *Journal of Lubrication Technology*, 92(3):466–472, July

1970. _eprint: https://asmedigitalcollection.asme.org/tribology/article-pdf/92/3/466/5795764/466_1.pdf.
- [46] Jung-Ping Liu, Wang-Yu Hsieh, Ting-Chung Poon, and Peter Tsang. Complex Fresnel hologram display using a single SLM. *Applied Optics*, 50(34):H128–H135, December 2011. Publisher: Optica Publishing Group.
- [47] Miles Padgett and Roberto Di Leonardo. Holographic optical tweezers and their relevance to lab on chip devices. *Lab on a Chip*, 11(7):1196–1205, 2011. Publisher: Royal Society of Chemistry.
- [48] Andreas Erik Gejl Madsen, René Lynge Eriksen, and Jesper Glückstad. Comparison of state-of-the-art Computer Generated Holography algorithms and a machine learning approach. *Optics Communications*, 505:127590, February 2022.
- [49] Hyosub Kim, Minhyuk Kim, Woojun Lee, and Jaewook Ahn. Gerchberg-Saxton algorithm for fast and efficient atom rearrangement in optical tweezer traps. *Optics Express*, 27(3):2184–2196, February 2019. Publisher: Optica Publishing Group.
- [50] Zhehai Zhou, Guoqing Hu, Shuang Zhao, Huiyu Li, and Fan Zhang. Holographic Optical Tweezers That Use an Improved Gerchberg-Saxton Algorithm. *Micromachines*, 14(5):1014, May 2023. Number: 5 Publisher: Multidisciplinary Digital Publishing Institute.
- [51] C. Maurer, A. Jesacher, S. Bernet, and M. Ritsch-Marte. What spatial light modulators can do for optical microscopy. *Laser & Photonics Reviews*, 5(1):81–101, 2011. _eprint: <https://onlinelibrary.wiley.com/doi/pdf/10.1002/lpor.200900047>.
- [52] Peter J. Christopher, George S. D. Gordon, and Timothy D. Wilkinson. Benchmarking the Gerchberg-Saxton Algorithm, May 2020. arXiv:2005.08623 [physics].
- [53] Xiaolei Peng, Zhihan Chen, Pavana Siddhartha Kollipara, Yaoran Liu, Jie Fang, Linhan Lin, and Yuebing Zheng. Opto-thermoelectric microswimmers. *Light: Science & Applications*, 9(1):141, August 2020. Number: 1 Publisher: Nature Publishing Group.

Code Availability. The relevant code to solve for pressure, integrate the ODE, and fit the data is included in the supplementary material.

Acknowledgements. The authors would like to thank Michael Reynolds and Matthew Campbell for helpful discussions, and the Singh Center for Nanotechnology staff for technical support during the fabrication process. The authors would also like to thank Professor Tom Mallouk, Professor Paulo Arratia, and Dr. Albane Théry for their comments on the manuscript. This work was supported by the Army Research Office (ARO YIP W911NF-17-S-0002) and the Air Force Office of Scientific Research (AFOSR FA9550-21-1-0313), and was carried out at the Singh Center for Nanotechnology, which is supported by the NSF National Nanotechnology Coordinated Infrastructure Program under grant NNCI-2025608.

Author Contributions. L.C.H., W.H.R., and M.Z.M designed the research. L.C.H. and W.H.R. designed and fabricated the robots. L.C.H. characterized the propulsion mechanism, with assistance from S.S. W.H.R. built the SLM system and programmed the control software, with assistance from T.S, and characterized the kinematics for two engine robots. M.Z.M. developed the fluid model and calculated numerical solutions for angle of attack and gap height, acquired funding, and supervised research. L.C.H., W.H.R., and M.Z.M. designed figures and wrote the manuscript.

Competing Interests. The authors declare no competing interests.

Data Availability. The authors declare that the data supporting the findings of this study are available within the paper and its supplementary information files. Source data are provided with this paper.

Additional Information. Supplementary information is available for this paper. Correspondence and requests for materials should be addressed to M.Z.M. Reprints and permissions information is available at www.nature.com/reprints.

3 Extended Data

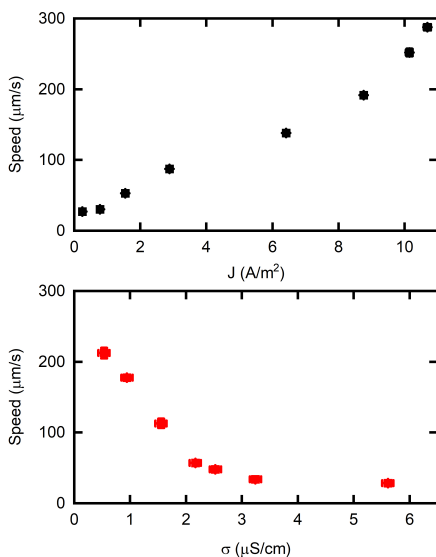


Fig. E1 Speed vs. current density and conductivity. Top: Robot speed as a function of current density for a fixed solution conductivity of 300 nS/cm in 5 mM hydrogen peroxide. Bottom: Robot speed as a function of conductivity in 5 mM hydrogen peroxide. Here current density also varies due to the changes in conductivity.

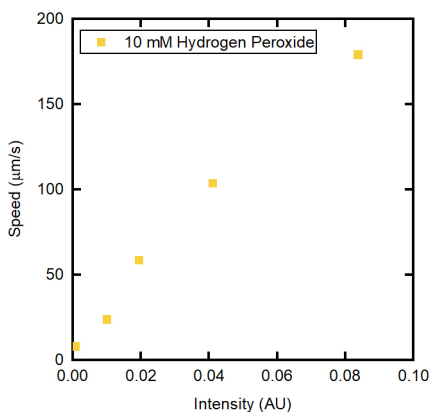


Fig. E2 Speed vs. intensity. Robot speed as a function of light intensity, i.e. optical power. For speeds below approximately $200 \mu\text{m/s}$ we find a linear relationship.

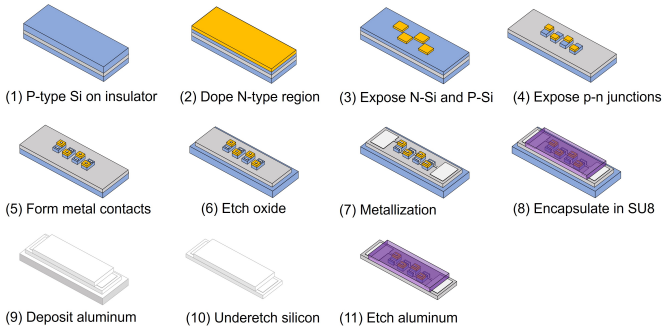


Fig. E3 Fabrication of a single motor. Steps (1)-(4) form discrete PVs through a series of doping and etching steps, Steps (5)-(7) deposit the electrical interconnects and actuator electrodes, and Steps (8)-(11) encapsulate and release the motors.

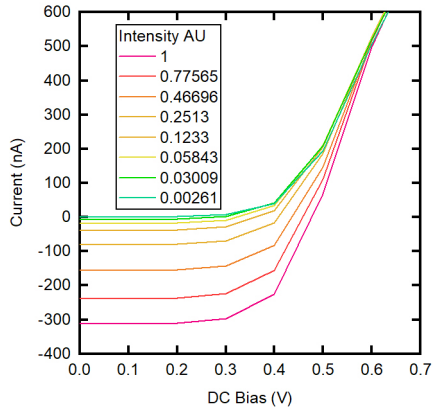


Fig. E4 PV I-V sweeps. Current vs voltage sweeps of a single PV under various illumination intensities, normalized to the maximum intensity of our light source.

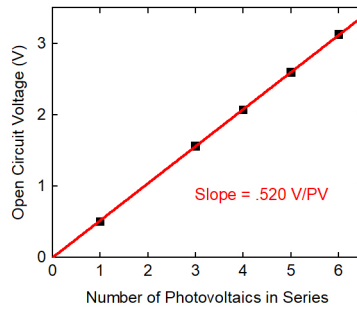


Fig. E5 Open circuit voltage. Open circuit voltage at maximum intensity as a function of the number of PVs wired in series.

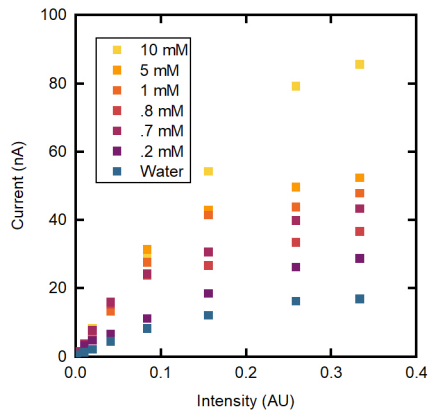


Fig. E6 PV output in different chemical environments. Current driven through various solutions by the PVs as a function of light intensity.

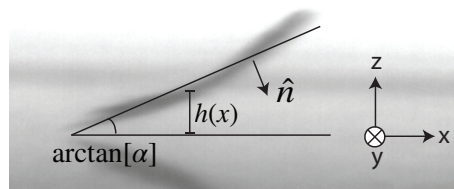


Fig. E7 Frame of reference for modeling propulsion. A schematic of the coordinates and approximation for geometry under the robot's body used in modeling the electric field and fluid flows.

4 Supplementary Information

Video 1

A single motor under microscope illumination. (This video is in real time).

Video 2

A single motor robot travels through an SU8 channel under microscope illumination. (This video is in real time).

Video 3

A side-on view of a two motor robot under illumination. Due to asymmetry in the motors, the robot drives in a circle. At the end of the video, the driving illumination is turned off and the robot stops moving. (This video is in real time).

Video 4

A controller autonomously pilots a robot to a waypoint by trimming the power on each engine. (This video has been sped up by 2x).

Video 5

A controller autonomously pilots a robot through a series of waypoints to trace out a Figure 8 pattern. (This video has been sped up by 2x).

Video 6

Given a list of target locations, robots autonomously travel to the nearest waypoint to form user-defined shapes. Shown here is a rectangle. (This video has been sped up by 2x).

Video 7

Given a different list of target locations, robots rearrange to form other user-defined shapes such as triangles. (This video has been sped up by 2x).

Video 8

Robots are assigned an individual list of waypoints to trace out separate paths simultaneously. (This video has been sped up by 2x).

Video 9

Robots are assigned dynamic waypoints such as the location of another robot in the system and form a chain-like structure in which they follow their nearest neighbor. Additionally, the controller prevents robots from getting too close

together, resulting in the stop-and-go behavior seen in this video. (This video has been sped up by 2x).